Experimental evidence of nonreciprocal propagation in space-time modulated piezoelectric phononic crystals

S. Tessier Brothelande, C. Croënne, F. Allein, Jerome O. Vasseur, M. Amberg, Frédéric Giraud, Bertrand Dubus

RESEARCH ARTICLE | NOVEMBER 13 2023

Experimental evidence of nonreciprocal propagation in space-time modulated piezoelectric phononic crystals

S. Tessier Brothelande ; C. Croënne ; F. Allein ; J. O. Vasseur ; M. Amberg; F. Giraud; B. Dubus

Appl. Phys. Lett. 123, 201701 (2023)
https://doi.org/10.1063/5.0169265

Applied Physics Letters ARTICLE pubs.aip.org/aip/apl

Experimental evidence of nonreciprocal propagation in space-time modulated piezoelectric phononic crystals

Cite as: Appl. Phys. Lett. **123**, 201701 (2023); doi: 10.1063/5.0169265
Submitted: 24 July 2023 · Accepted: 25 October 2023 ·
Published Online: 13 November 2023

S. Tessier Brothelande,[1,a] C. Croënne,[1] F. Allein,[1] J. O. Vasseur,[1] M. Amberg,[2] F. Giraud,[2] and B. Dubus[1]

AFFILIATIONS

[1]Univ. Lille, CNRS, Centrale Lille, Univ. Polytechnique Hauts-de-France, Junia, UMR 8520 – IEMN, F-59000 Lille, France
[2]L2EP INRIA Futurs, University of Lille, Villeneuve d'Ascq, France

[a]Author to whom correspondence should be addressed: sarah.tessier@cnrs.fr

ABSTRACT

A nonreciprocal system composed of a one-dimensional piezoelectric phononic crystal whose periodic electrical conditions are modulated in time is presented. One-way longitudinal wave propagation is studied experimentally and compared to finite element temporal simulations. The modulation is performed by prescribing grounded or floating potential conditions on a periodic set of electrodes through external circuits. This approach makes it possible to consider a wide range of modulation speeds, and the large number of unit cells of the phononic crystal allows us to characterize experimentally the full dispersion curves of the system. This permits to observe the presence of directional bandgaps and to follow the shift in frequencies of these bandgaps as a function of the modulation speed. The experiments show the linear evolution of the central position of the bandgaps with the increase in the modulation speed, as well as their progressive closure, over a wide range of frequencies. Experiments are also used to estimate the evolution of bandgaps in a dispersive system, a problem discussed in several theoretical works but never observed experimentally. This work may constitute the foundation for experimental analysis of Floquet acoustic metamaterials, accelerated-modulation space-time metamaterials, or acoustic analog of the event horizon.

To break reciprocity of acoustic wave propagation, non-Hermitian systems based on three physical mechanisms have been considered in recent years: (i) nonlinear propagation in nonsymmetric layered media causing rectification of energy flux due to nonreciprocal energy dissipation at harmonic frequencies;[1,2] (ii) introduction of a static bias generated by a circulating fluid[3] to realize sound wave circulators[4] or isolators;[5] and (iii) time-varying acoustic materials with prescribed time modulation,[6] locally time-controlled or time-programmable properties[7–10] or space-time modulation. Most theoretical and numerical studies on space-time modulated (STM) acoustic metamaterials focus on acoustic or elastic media with sinusoidal space-time modulation of an elastic parameter, typically Young's modulus,[11–14] bulk modulus,[15] or shear modulus.[16] They report tilting of dispersion curves and nonreciprocal dispersion similar to those described by Cassedy and Oliner in their seminal work on space-time modulated electromagnetic waveguides.[17] STM acoustic metamaterials are a specific type of time-varying media or Floquet metamaterials, which have been identified as a unique opportunity to design novel forms of wave–mater interaction.[18,19] One advantage of STM metamaterials lies in the introduction of additional time/frequency and space/wavenumber scales associated with the modulation which may couple to wave frequency/wavenumber and metamaterial resonance frequency. The broad spectrum of these interactions eventually associated with multiphysical and/or nonlinear effects constitutes a rising field of research for wave engineering. Uniform-velocity space-time crystals[20] is a kind of STM metamaterial, including a periodic sequence of space-time discontinuities, which exhibit theoretically in the elastic case nonreciprocity and macroscopic behavior of a Willis medium at low modulation speed.[21]

Practical realizations of STM systems rely on space-time control of electric boundary conditions applied to magnetic or piezoelectric elements in order to modify locally the properties of a waveguide. Magnetic systems using coils and magnets arranged on rails[22] or resonators composed of coils with modulated electric currents[23] are realized with a rather limited number of unit cells (4–6), allowing only the study of transmission signal through small slabs. Another system is developed using piezoelectric patches arranged on an elastic substrate to constitute a slab of eight cells submitted to a square modulation.[24]

In this complex structure, each piezoelectric element is separately connected to its own independent circuit. The dispersion diagrams are evaluated around the directional bandgaps in a narrow frequency band. To improve the effective electromechanical coupling of the structure, spatiotemporal modulation is realized with switchable negative capacitance shunts. Although shunted piezoelectric patches can operate over a wide range of frequencies, the circuits can become unstable due to the use of negative capacitances.[24,25]

In this Letter, we report the development of an experimental setup enabling the measurement of the full dispersion diagram of a STM metamaterial. We study the propagation of elastic waves in a piezoelectric phononic crystal (PC) made up of about one hundred identical piezoelectric elements separated by thin electrodes as depicted in Fig. 1(a). The relation between mechanical and electrical quantities in the case of a long rod polarized along its length is given by

$$T_3(z) = c_{33}^D S_3(z) + e_{33} D_3(z), \tag{1}$$

where S_3, T_3, and D_3 are the mechanical strain, the mechanical stress, and the electric displacement along the z axis, respectively. c_{33}^D and e_{33} are the elastic compliance constant at constant electric displacement and the piezoelectric stress constant, respectively. Electrodes are supposed to have a negligible mechanical effect on wave propagation provided that they are thin enough with respect to wavelength. For an electrode with zero surface charge density (a floating potential),

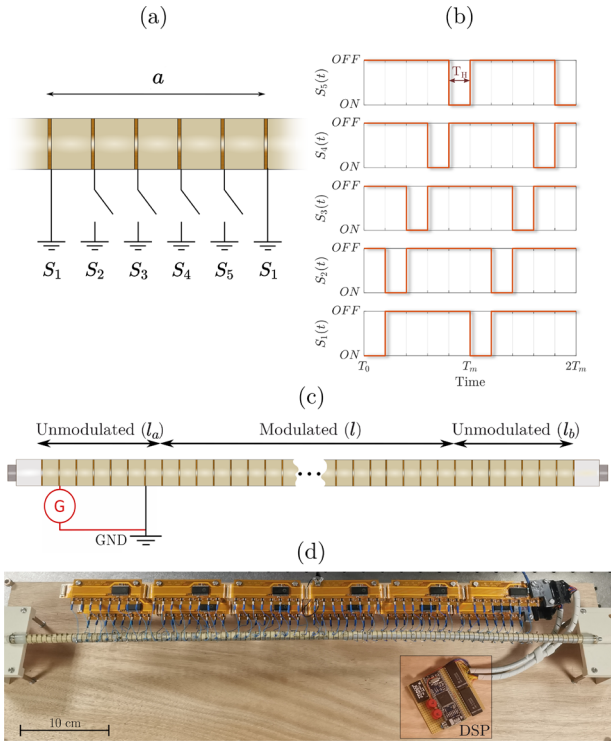

FIG. 1. (a) Schematic view of electrical boundary conditions imposed to electrodes of one cell ($N = 5$). (b) Command law of the switches S vs time. (c) Schematic view of the stack including the source, the modulated (l), and unmodulated regions of length l_a (where excitation is generated) and l_b (where electrodes are left floating). (d) Picture of the experimental setup of space-time modulation of electrical conditions imposed to the electrodes through DRAM memories controlled by the DSP.

Gauss's law leads to the continuity of electrical displacement through the interface and consequently to the continuity of the mechanical strain as T_3 should be continuous. Therefore, the acoustic wave is fully transmitted through the electrodes. Conversely, for a grounding condition, a discontinuity of the electrical displacement may appear between two piezoelectric elements if electrical charges move from ground to the electrode. In this case, an impedance mismatch takes place at the interface and the acoustic wave is partly reflected and transmitted. Then, the propagation of mechanical waves in a piezoelectric medium depends on prescribed electrical boundary conditions and a periodic grounding of the electrodes introduces a Bragg bandgap which does not exist when the electrodes have a floating potential condition.[26] When the electrical conditions of the electrodes are modulated both in space and in time in such a piezoelectric structure, wave dispersion is strongly modified and becomes nonreciprocal.[27,28]

This system allows a very simple and fast enough space-time modulation of the boundary conditions well suited for an experimental implementation. It is composed of a large number of controllable elements to obtain full dispersion curves with adequate wavenumber resolution and experimental range. In addition, wave propagation in the piezoelectric material provides sufficient modulation-wave coupling to use simple electronic circuits for the modulation. Thus, very fast modulation speeds can be obtained without stability issues. Moreover, as electrical conditions are carried out using external circuits, it is also possible to apply different types of modulation, other than a shift of the electrical conditions at constant speed. In this paper, we focus on the study of a control law with a constant modulation speed in the subsonic regime, i.e., a modulation speed c_m lower than the velocity of the propagating waves of the system c_L.

The experimental setup is composed of a stack of 113 piezoelectric rings polarized along their length separated by 114 thin electrodes. The latter are made of brass of density $\rho_l = 8550$ kg/m^3 and Young's modulus $E_l = 100$ GPa. The piezoelectric rings are made of lead zirconate titanate (PZT) with density $\rho_p = 7650$ kg/m^3 and elastic stiffness modulus at constant electric field $c_{33}^D = 41.8$ GPa, leading to a longitudinal wave velocity of $c_L = \sqrt{c_{33}^D/\rho_p} = 3479$ ms^{-1}. The dimensions of the rings and electrodes are given in Table I.

The modulation of the electrical conditions is performed using switches that set electrodes to ground or to floating potential. The switches state is defined by a digital signal processor (DSP). Dynamic random access memories (DRAMs) allow to deliver logical values to each switch to dictate its state as a function of time. The modulation is performed by shifting the position of the periodic set of grounding conditions in time [Figs. 1(a) and 1(b)]. 95 electrodes are connected to switches and form the modulated region of length l, as represented Fig. 1(c). Unmodulated regions are placed at the two stack ends. The left one, where the excitation is generated, is of length l_a. In the right

TABLE I. Dimensions of the piezoelectric rings and electrodes used in the phononic crystal assembly.

Elements	Outer radius (mm)	Inner radius (mm)	Thickness (mm)
Piezoelectric rings	$r_{ex} = 5$	$r_{in} = 3$	$e_p = 5$
Electrodes	$r_{ex} = 5$	$r_{in} = 3$	$e_l = 0.5$

one, of length l_b, all the electrodes are left floating. A picture of the stack and its external circuits is displayed in Fig. 1(d).

The switches are operated at a modulation period T_m that dictates the modulation speed $c_m = \frac{a}{T_m}$ with a the spatial period corresponding to the minimum distance between two successive grounded electrodes as depicted in Fig. 1(a). Although the spatiotemporal modulation is naturally described by a modulation speed, the modulation frequency $f_m = \frac{c_m}{a}$ is defined by the number of times a given periodic space distribution is met per second. Grounding one electrode out of N is equivalent to a spatial period $a = N(e_p + e_l)$, leading to about $95/N$ cells in the phononic crystal slab. The position of the grounded electrodes is shifted every $T_H = T_m/N$, returning to their initial position every T_m. In this paper, we consider two cases: for $N = 5$, a slab composed of 19 cells submitted to a five step modulation; for $N = 3$, a slab of 30 cells submitted to a three step modulation.

Elastic waves are generated by applying a voltage difference between two electrodes separated by five piezoelectric rings located in the left unmodulated region. The source signal is a frequency chirp between 1 and 120 kHz. An external trigger synchronously starts the modulation, the excitation, and the acquisition system in order to have same phase reference for each measurement. The dispersion curves are characterized experimentally by measuring the electrical potential of each electrode as a function of time.[29] Measurements of electrical potentials are made automatically with a data acquisition system (DAQ). They last 10 ms, a duration much larger than T_m and than the round trip time of flight of the acoustic wave in the PC slab. A space-time Fourier transform is then applied to these measurements in order to calculate the corresponding experimental dispersion curves.

The longitudinal wave velocity found experimentally when all electrodes are floating is $c_L = 3210$ ms^{-1}, lower than that calculated theoretically from the material constants of the piezoelectric elements. This difference originates mainly from the electrical circuits of the DSP and the DAQ which introduce parasitic capacitances. Previous theoretical analysis of piezoelectric phononic crystals demonstrated that these additional capacitances modify the wave velocity and the effective coupling coefficient.[30]

We consider first the case $N = 5$ with a spatial period $a = 27.5$ mm, corresponding to every fifth electrode being grounded with a resulting bandgap centered around 57.4 kHz. Experimental results for modulation speeds of 0, 500, and 1000 ms^{-1} are shown in Fig. 2, for the first two Brillouin zones and frequencies up to 120 kHz. High amplitudes (bright yellow spots) correspond to the longitudinal vibration modes of the structure. The positions in frequency and wave number of the unmodulated bandgap are marked by horizontal and vertical dotted lines. The previously mentioned parasitic capacitances strongly reduce the bandgap widths by shifting down their upper limit so much that they can no longer be identified clearly. However, bandgap center frequency may still be identified by the crossings of dispersion branches.

In this study, we analyze the shift in frequency and wavenumber of these crossings (identified with blue markers in Fig. 2) for a nonvanishing value of k as a function of modulation speed. The positive and negative wavenumber intersections shift to the higher and lower frequencies, respectively. The longitudinal mode has a dispersive branch above 100 kHz due to a strong coupling with the radial mode of the rings, present at higher frequencies.

Several theoretical works[17,20] have established that center frequency f_s of shifted bandgap and reduced wave number $k_s a/\pi$ at the crossing points exhibit linear dependencies with the modulation speed given by the following expressions:

$$f_s = \pm \frac{c_m + c_L}{2a}, \quad \frac{k_s a}{\pi} = \pm 1 + \frac{c_m}{c_L}. \tag{2}$$

For the experiments, the position of the crossings is followed for modulation speeds ranging from $c_m = 0$ to $c_m = 2000$ ms^{-1} by steps of $c_m = 100$ ms^{-1}. The same process is applied to finite element temporal

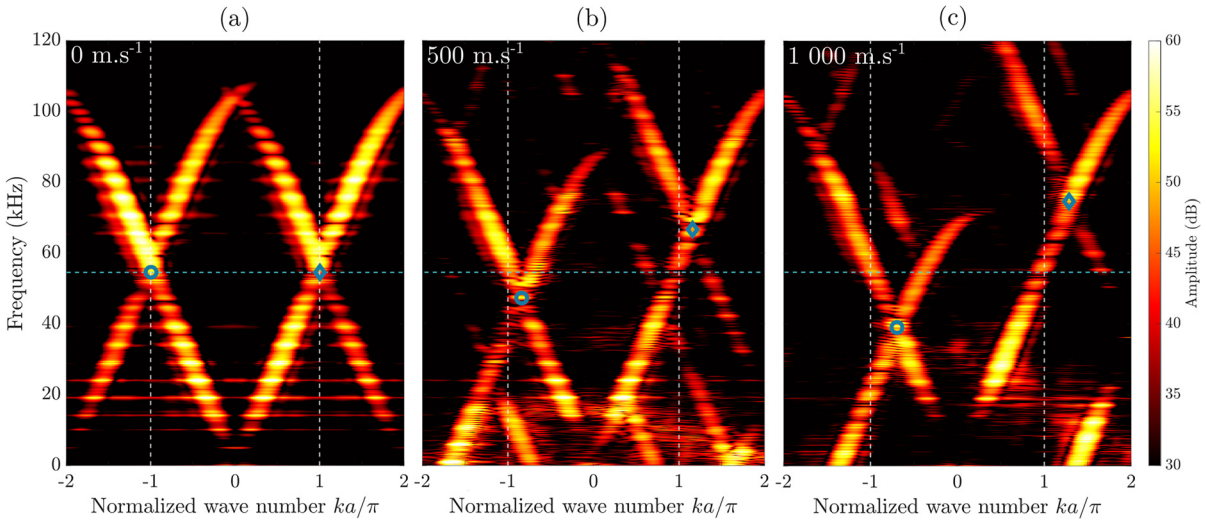

FIG. 2. Space-time Fourier transform of electrodes electrical potential measurements for a modulation speed of (a) $c_m = 0$, (b) $c_m = 500$, and (c) $c_m = 1000$ ms^{-1} for a spatial period $a = 27.5$ mm corresponding to one in five grounded electrodes. As a reference, the position in frequency and wave number of the crossings of dispersion branches in the static ($c_m = 0$ ms^{-1}) case is overlapped on all graphs with dashed lines. An animated view of these experimental results for modulation speeds ranging from 0 to 2000 ms^{-1} is provided in the supplementary material.

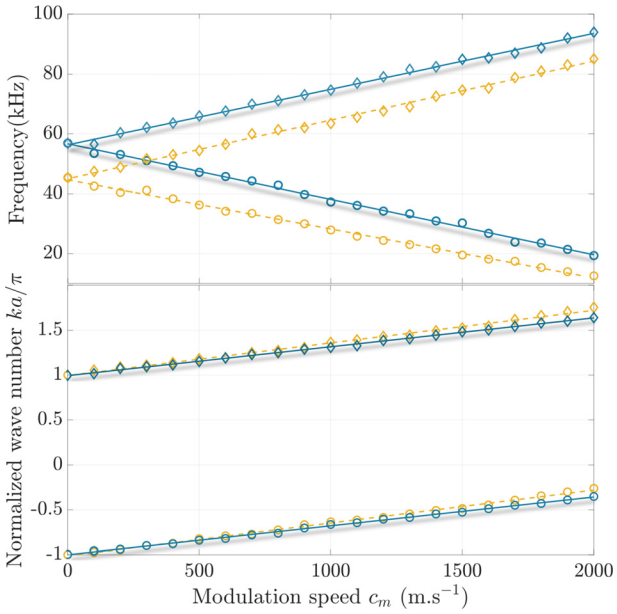

FIG. 3. Variation of the position in frequency and normalized wave number of crossings of dispersion branches (such as those shown in Fig. 2) as a function of the modulation speed for experimental (blue) and simulation (yellow) results. Tracking of negative (positive) wavenumber bandgap is represented by diamond-shaped (circle) markers. A linear regression is represented in dotted (plain) lines on simulation (experimental) results.

simulations results carried out with Comsol software. The description and parameters of the simulations are given in the supplementary material (S2). Figure 3 displays the position of the crossings in frequency and normalized wave number vs the modulation speed. The distribution of the measurements confirms the linear character of the evolution of crossings position in frequency and wavenumber up to a modulation speed of $c_m = 2000$ ms^{-1} $= 0.62c_L$. This evolution is of the same nature for finite element simulations. The slope of the linear regression of frequency positions is ± 18.45 m^{-1} for the experiments and ± 18.18 m^{-1} for simulations results. The latter value corresponds exactly to the theoretical value $\pm 1/2a$. A good agreement between the experimental and numerical results is found, with a slightly smaller slope for the numerical results. The frequency shift of 11.48 kHz between simulation and experimental results is mainly due to the mechanical contact between elements: in the simulations, a perfect contact is assumed, implying a higher effective coupling coefficient than the experiments and, thus, a downshift of the lower limit of the bandgap. Further explanations are provided in the supplementary material. The wavenumber shift of the two intersections is linear as well, with a slightly higher slope for simulation results. Nevertheless, the overall excellent agreement between measurements and theoretical predictions confirms the reliability of the experimental setup to exhibit phenomena associated with temporal modulations of waveguide properties.

We consider now the case $N = 3$ with a spatial period $a = 16.5$ mm, corresponding to every third electrode being grounded with a resulting bandgap between $f_{min} = 89.3$ and $f_{max} = 95.6$ kHz. In this case, the measurements are made with an oscilloscope which allows to greatly reduce the parasitic capacitances and, therefore, to avoid total bandgap closure. Additionally, the longitudinal wave velocity for floating potentials found experimentally is then $c_L = 3390$ ms^{-1}, much closer to the theoretical value. Elastic waves are generated in the same fashion as for the $N = 5$ case. Source signal is a Ricker pulse $x(t) = A(1 - 2\pi^2 f_0^2 t^2)e^{-(\pi f_0 t)^2}$ centered at $f_0 = 50$ kHz.

Results obtained for modulation speeds of 0, 100, and 200 ms^{-1} are displayed in Fig. 4. Curves are represented up to 120 kHz for frequency and up to the first two Brillouin zones for normalized wavenumbers. As expected from previous theoretical works,[27,28] the bandgap initially located at a positive (negative) wavenumber has shifted up (down) in frequency and shifted to positive wavenumbers. At $c_m = 100$ ms^{-1}, there is no frequency overlap between both bandgaps meaning that they can be identified as directional. The bandgaps

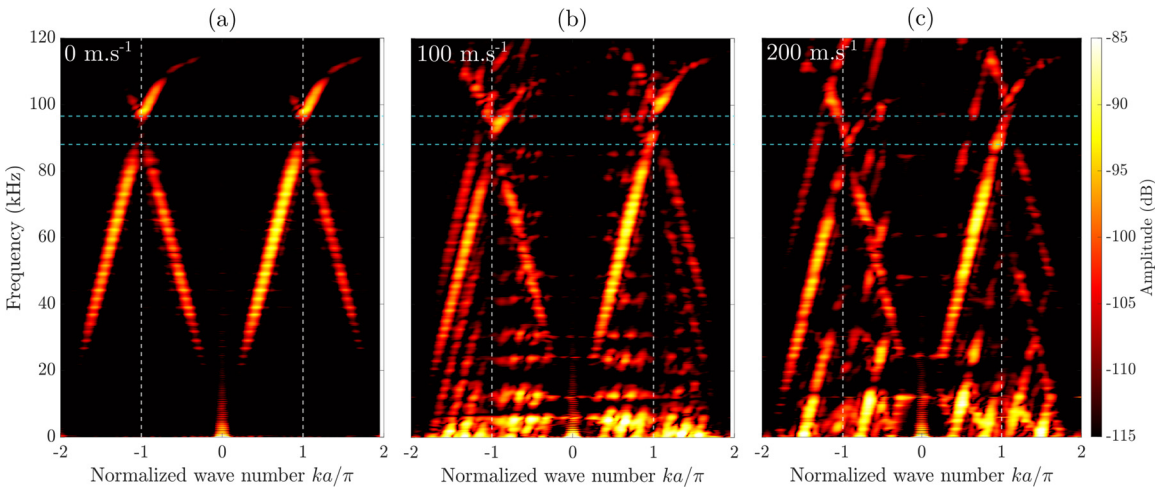

FIG. 4. Space-time Fourier transform of electrodes electrical potential measurements for a modulation speed of (a) $c_m = 0$, (b) $c_m = 100$, and (c) $c_m = 200$ ms^{-1} for a spatial period $a = 16.5$ mm corresponding to one in three grounded electrodes. The position in frequency and wavenumber of the bandgap in the static ($c_m = 0$ ms^{-1}) case is overlapped on all graphs with dashed lines.

are getting narrower as the modulation speed increases, from 7.5 kHz width for $c_m = 0$ ms^{-1} to 5.4 kHz for $c_m = 100$ ms^{-1}, until getting almost completely closed for $c_m = 200$ ms^{-1}.

Additional branches, parallel to the main curves, are observed due to the discrete nature of the modulation that introduces other modulation speeds defined by $c_m^n = (1 + N.n)c_m$ with n being a relative integer and $N = 3$ being the number of electrodes in the unit cell. In this case, a shift of speed c_m is equivalent to a shift of $c_m^{-1} = -2c_m$ and $c_m^1 = 4c_m$ among others. These satellite branches are a vertical translation of the dispersion curves equal to modulation rates $f_m^n = \frac{c_m^n}{a}$ and, thus, quickly move away from the studied frequency band. It should be noted that these additional branches are also present in the experiments with $N = 5$ but with a lower amplitude.

The case $N = 3$ is particularly interesting for measuring bandgap evolution in a dispersive system. Figure 5 shows the tracking of the position in frequency of the upper and lower limits of the experimental bandgaps. Black dashed lines are linear interpolations between two successive measurement points used to guide interpretation. Diagrams for negative values of c_m are obtained by tracking the negative wavenumber bandgap using the back-scattered waves with respect to modulation direction. Indeed, the evolution of the negative wavenumber bandgap corresponds to that of the positive wavenumber bandgap for a modulation speed of opposite sign. Results show that bandgap evolution is no longer linear with the modulation speed as they take place in the dispersive branch of the mode. The measurements also display a strong narrowing of bandgap with modulation speed which vanish completely for $c_m = \pm 400$ ms^{-1}.

This gap narrowing effect is in qualitative agreement with previously published analytical and numerical results,[27,28] even though it is much more pronounced here (see Sec. 4 of the supplementary material). One possible explanation for this difference lies in the influence of the strong hybridization with the radial mode present at slightly higher frequencies, which was not considered in previous models. The interplay between the main bandgap and this hybridization gap should depend strongly on the modulation speed, since the former is closely related to the modulation, while the latter is a consequence of the (constant) lateral dimension of the piezoelectric rings.

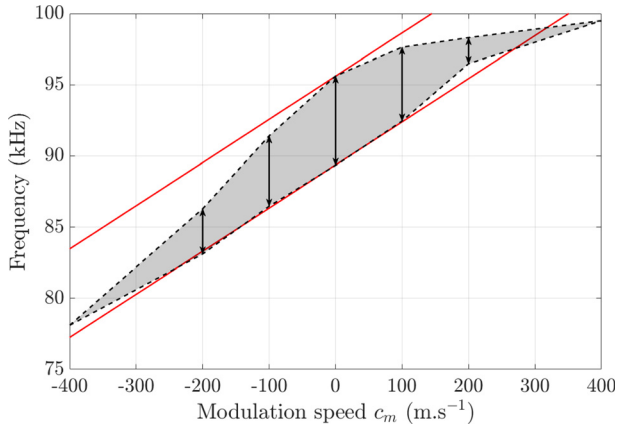

FIG. 5. Variation of bandgap frequency limits with the modulation speed. Measurement points are represented by black arrows and analytical points for an equivalent modulated bi-layer in red.

Additionally, it should be noted that these gap narrowing effects are almost completely absent for other classes of STM systems, such as one-dimensional elastic bi-layer crystals composed of nondispersive layers with interfaces moving at constant speed.[20,21] As a reference, Fig. 5 displays the calculated variation of bandgap frequency limits with modulation speed for a STM bi-layer crystal having the same spatial period $a = 16.5$ mm and same wave velocities $c_1 = c_2 = 3052$ ms^{-1} than the experimental setup, but with different densities ($\rho_1 = 7650$ and $\rho_1 = 6880$ kg m^{-3}) chosen in order to fit the experimental bandgap for $c_m = 0$ ms^{-1}.

The experimental implementation of a STM piezoelectric phononic crystal combined with the fast modulation of electrical conditions through external circuits gives direct access to full dispersion curves. It may easily be adapted to more complex modulation laws and to supersonic modulation speeds. Thereby, it paves the way to the experimental analysis of Floquet acoustic metamaterials,[18] accelerated-modulation space-time metamaterials,[31] or acoustic analog of the event horizon.[32]

See the supplementary material for additional information including the full description of the experimental setup and measurements (S1), finite element simulations description, experimental and simulated wave-fields as well as dispersion curves for higher modulation speeds (S2), the PC mode shapes (S3), analytical results (S4), and transmission spectra (S5).

This work was supported by the French Agence Nationale de la Recherche (MEANDRE ANR-18-CE08-0007-01).

AUTHOR DECLARATIONS

Conflict of Interest

The authors have no conflicts to disclose.

Author Contributions

Sarah Tessier Brothelande: Data curation (equal); Formal analysis (equal); Investigation (equal); Methodology (equal); Software (equal); Visualization (equal); Writing – original draft (lead); Writing – review & editing (lead). **Charles Croënne:** Conceptualization (equal); Formal analysis (equal); Funding acquisition (equal); Methodology (equal); Software (equal); Supervision (equal); Validation (equal); Visualization (equal); Writing – review & editing (supporting). **Florian Allein:** Data curation (equal); Writing – review & editing (supporting). **Jerome Vasseur:** Validation (equal); Writing – review & editing (supporting). **Michel Amberg:** Software (equal). **Frédéric Giraud:** Software (equal). **Bertrand Dubus:** Conceptualization (equal); Project administration (equal); Supervision (equal); Validation (equal); Writing – original draft (supporting); Writing – review & editing (supporting).

DATA AVAILABILITY

The data that support the findings of this study are available within the article and its supplementary material.

REFERENCES

[1]B. Liang, B. Yuan, and J-c Cheng, "Acoustic diode: Rectification of acoustic energy flux in one-dimensional systems," Phys. Rev. Lett. **103**, 104301 (2009).
[2]B. Liang, X. Guo, J. Tu, D. Zhang, and J. Cheng, "An acoustic rectifier," Nat. Mater. **9**, 989–992 (2010).

[3]F. Zangeneh-Nejad and R. Fleury, "Doppler-based acoustic gyrator," Appl. Sci. **8**, 1083 (2018).
[4]R. Fleury, D. Sounas, C. Sieck, M. Haberman, and A. Alù, "Sound isolation and giant nonreciprocity based on the acoustic Zeeman effect," Science **343**, 516–519 (2014).
[5]C. P. Wiederhold, D. L. Sounas, and A. Alù, "Nonreciprocal acoustic propagation and leaky-wave radiation in a waveguide with flow," J. Acoust. Soc. Am. **146**, 802–809 (2019).
[6]N. Swinteck, S. Matsuo, K. Runge, J. O. Vasseur, P. Lucas, and P. A. Deymier, "Bulk elastic waves with unidirectional backscattering-immune topological states in a time-dependent superlattice," J. Appl. Phys. **118**, 063103 (2015).
[7]A. Baz, "Active nonreciprocal acoustic metamaterials using a switching controller," J. Acoust. Soc. Am. **143**, 1376–1384 (2018).
[8]Y. Zhai, H.-S. Kwon, and B.-I. Popa, "Active Willis metamaterials for ultracompact nonreciprocal linear acoustic devices," Phys. Rev. B **99**, 220301 (2019).
[9]A. Baz, "Active nonreciprocal metamaterial using an eigen-structure assignment control strategy," J. Acoust. Soc. Am. **147**, 2656–2669 (2020).
[10]C. Cho, X. Wen, N. Park, and J. Li, "Digitally virtualized atoms for acoustic metamaterials," Nat. Commun. **11**, 251 (2020).
[11]G. Trainiti and M. Ruzzene, "Non-reciprocal elastic wave propagation in spatio-temporal periodic structures," New J. Phys. **18**, 083047 (2016).
[12]K. Yi, S. Karkar, and M. Collet, "One-way energy insulation using time-space modulated structures," J. Sound Vib. **429**, 162–175 (2018).
[13]E. Riva, J. Marconi, G. Cazzulani, and F. Braghin, "Generalized plane wave expansion method for non-reciprocal discretely modulated waveguides," J. Sound Vib. **449**, 172–181 (2019).
[14]J. Palacios, L. Calderin, A. Chon, I. Frankel, J. Alqasimi, F. Allein, R. Gorelik, T. Lata, R. Curradi, G. Lambert-Milak *et al.*, "Temperature-controlled spatiotemporally modulated phononic crystal for achieving nonreciprocal acoustic wave propagation," J. Acoust. Soc. Am. **151**, 3669–3675 (2022).
[15]H. Nassar, H. Chen, A. Norris, and G. Huang, "Quantization of band tilting in modulated phononic crystals," Phys. Rev. B **97**, 014305 (2018).
[16]M. B. Zanjani, A. R. Davoyan, A. M. Mahmoud, N. Engheta, and J. R. Lukes, "One-way phonon isolation in acoustic waveguides," Appl. Phys. Lett. **104**, 081905 (2014).
[17]E. S. Cassedy and A. A. Oliner, "Dispersion relations in time-space periodic media: Part I. Stable interactions," Proc. IEEE **51**, 1342–1359 (1963).
[18]S. Yin, E. Galiffi, and A. Alù, "Floquet metamaterials," ELight **2**, 1–13 (2022).
[19]E. Galiffi, R. Tirole, S. Yin, H. Li, S. Vezzoli, P. A. Huidobro, M. G. Silveirinha, R. Sapienza, A. Alù, and J. Pendry, "Photonics of time-varying media," Adv. Photonics **4**, 014002 (2022).
[20]Z.-L. Deck-Léger, N. Chamanara, M. Skorobogatiy, M. G. Silveirinha, and C. Caloz, "Uniform-velocity spacetime crystals," Adv. Photonics **1**, 056002 (2019).
[21]H. Nassar, X. Xu, A. Norris, and G. Huang, "Modulated phononic crystals: Non-reciprocal wave propagation and Willis materials," J. Mech. Phys. Solids **101**, 10–29 (2017).
[22]Y. Wang, B. Yousefzadeh, H. Chen, H. Nassar, G. Huang, and C. Daraio, "Observation of nonreciprocal wave propagation in a dynamic phononic lattice," Phys. Rev. Lett. **121**, 194301 (2018).
[23]Y. Chen, X. Li, H. Nassar, A. N. Norris, C. Daraio, and G. Huang, "Nonreciprocal wave propagation in a continuum-based metamaterial with space-time modulated resonators," Phys. Rev. Appl. **11**, 064052 (2019).
[24]J. Marconi, E. Riva, M. Di Ronco, G. Cazzulani, F. Braghin, and M. Ruzzene, "Experimental observation of non-reciprocal band-gaps in a space-time modulated beam using a shunted piezoelectric array," Phys. Rev. Appl. **13**, 031001 (2020).
[25]F. Tateo, M. Collet, M. Ouisse, M. Ichchou, K. Cunefare, and P. Abbé, "Experimental characterization of a bi-dimensional array of negative capacitance piezo-patches for vibroacoustic control," J. Intell. Mater. Syst. Struct. **26**, 952–964 (2015).
[26]S. Degraeve, C. Granger, B. Dubus, J. O. Vasseur, M. Pham Thi, and A.-C. Hladky-Hennion, "Bragg band gaps tunability in an homogeneous piezoelectric rod with periodic electrical boundary conditions," J. Appl. Phys. **115**, 194508 (2014).
[27]C. Croënne, J. O. Vasseur, O. Bou Matar, M.-F. Ponge, P. Deymier, A.-C. Hladky-Hennion, and B. Dubus, "Brillouin scattering-like effect and non-reciprocal propagation of elastic waves due to spatio-temporal modulation of electrical boundary conditions in piezoelectric media," Appl. Phys. Lett. **110**, 061901 (2017).
[28]C. Croënne, J. O. Vasseur, O. Bou Matar, A.-C. Hladky-Hennion, and B. Dubus, "Non-reciprocal behavior of one-dimensional piezoelectric structures with space-time modulated electrical boundary conditions," J. Appl. Phys. **126**, 145108 (2019).
[29]F. Chikh-Bled, N. Kherraz, R. Sainidou, P. Rembert, and B. Morvan, "Piezoelectric phononic plates: Retrieving the frequency band structure via all-electric experiments," Smart Mater. Struct. **28**, 115046 (2019).
[30]S. Degraeve, C. Granger, B. Dubus, J. O. Vasseur, M. P. Thi, and A.-C. Hladky, "Tunability of Bragg band gaps in one-dimensional piezoelectric phononic crystals using external capacitances," Smart Mater. Struct. **24**, 085013 (2015).
[31]A. Bahrami, Z.-L. Deck-Léger, and C. Caloz, "Electrodynamics of accelerated-modulation space-time metamaterials," Phys. Rev. Appl. **19**, 054044 (2023).
[32]T. G. Philbin, C. Kuklewicz, S. Robertson, S. Hill, F. Konig, and U. Leonhardt, "Fiber-optical analog of the event horizon," Science **319**, 1367–1370 (2008).